Performance Analysis of Nested-loop Secondary Linear Doubly-fed Machine Considering End Effects

Yaping Zhang, Jian Ge, Wei Xu, *Senior Member, IEEE*, Weiye Li, Yinglu Luo, Shihu Su, and Yunfeng He

***Abstract*—Nested-loop secondary linear doubly-fed machine (NLS-LDFM) is a novel linear machine evolved from rotary brushless doubly-fed induction machine, which has a good application prospect in linear metro. In order to analyze the performance of NLS-LDFM, the mechanism and action rules of end effects are investigated in this paper. Firstly, the mechanism of static and dynamic end effects is analyzed in aspect of direct coupling, winding asymmetry and transient secondary current. Furthermore, based on the winding theory for short primary linear machines, the machine parameters are established qualitatively considering pulsating magnetic field of NLS-LDFM. Finally, the NLS-LDFM performance analysis is supplemented by the finite element algorithm (FEA) simulation and experiments under different operating conditions.**

***Index Terms*—Linear doubly-fed machine (LDFM), End effect, Parameter analysis, Finite element algorithm (FEA).**

I. Introduction

NEST-LOOP secondary linear doubly-fed machine (NLS-LDFM) comprises two sets of windings embedded in the same primary iron core with different pole-pair number, named power winding (PW) and control winding (CW), respectively. The magnetic fields generated by primary windings are modulated by the nested-loop secondary (NLS) with proper design, which leads to the indirect coupling between PW and CW. The fundamental topology of NLS-LDFM is shown in Fig. 1. Compared with the LIM driven system, NLS-LDFM drive system has some superiors, such as more adjustable power factor, stronger traction, *etc*. Meanwhile, the nested-loop embedded in the long secondary is a short-circuit structure without external power supply, which can reduce the cost of production and maintenance. Hereby, NLS-LDFM has the potential to be applied in urban rail transit

The NLS-LDFM is firstly proposed by Oregon State University, which consists of 1/3 pole-pairs stator windings and nested-loop secondary [1]. And the magnetic field and thrust ripple of NLS-LDFM are analyzed [20], [21]. However, the above methods still have limitations for analyzing NLS-LDFM because the transient secondary current in the process of nested-loop passing through the magnetic field is ignored. Although the structure of NLS-LDFM has been proposed for many years, the end effect research for NLS-LDFM is still in the initial stage.

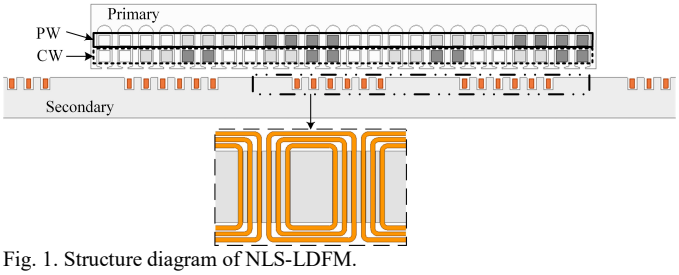

Fig. 1. Structure diagram of NLS-LDFM.

In general, the end effect also exists in other topologies of linear machines. The doubly-fed flux-switching linear machine (DFFSLM) is studied by Nanjing University of Aeronautics and Astronautics [3] and Zhejiang University [10], [11]. And the double-side excited linear doubly-fed machine (DSE-LDFM) with a long primary is mainly studied by University of Paderborn [4]-[6], the Delft University of Technology [7], Southwest Jiaotong University [8], and Tongji University [9]. However, due to the distinctive differences of topology and operation principle, the research on end effect in DFFSLM and DSE-LDFM is not available for the NLS-LDFM. For the linear inductance machine (LIM) [12], [13], the electroconductivity of secondary plate is constant and continuous along the motion direction [14], [15]. Thus, the end effect of LIM is commonly analyzed by solving Maxwell equations [16]. However, the property of NLS is different from that of secondary plate in LIM, thereof the analytical methods of end effects in LIM are not applicable for the NLS-LDFM.

For this paper, the static and dynamic end effects in the NLS-LDFM are investigated. The main contents are organized as follows. In Section II, the mechanism and action rules of the static and dynamic end effects are revealed. In Section III, the fundamental parameters of NLS-LDFM are analyzed qualitatively. In Section IV, combined with the theoretical analysis, the end effects on the NLS-LDFM performances are

Manuscript received April 19, 2022; revised March 10, 2022; accepted March 14, 2022. date of publication September 25, 2022; date of current version September 18, 2022

This work was supported in part by the National Natural Science Foundations of China under Grants 52277050 and 51877093, the fund from Science, Technology, Shenzhen International Collaboration under Grant GJHZ20210705142539007, the Key Research and Development Program of Sichuan Province under Grant 2021YFG0081, and the fund from Science, Technology and Innovation Commission of Shenzhen Municipality under Grant JCYJ20190809101205546. *(Corresponding Author: Ge, Jian)*

Yaping Zhang, Jian Ge (Corresponding author), and Wei Xu are with the State Key Laboratory of Advanced Electromagnetic Engineering and Technology, School of Electrical and Electronic Engineering, Huazhong University of Science and Technology, Wuhan 430074, China (e-mails: yapingzhang@hust.edu.cn, gejian1994@hust.edu.cn, weixu@hust.edu.cn).

Weiye Li and Yinglu Luo are with Xiangyang CRRC Zhuzhou Institute CO., LTD, Xiangyang, 412001, China (e-mails: liwy@csrzic.com, luoyl@csrzic.com).

Shihu Su and Yunfeng He are with the CRRC Zhuzhou Motor Co., Ltd., Zhuzhou, 412001, China (e-mails: sushihu@crrcgc.com, yunfeng-he@163.com).

Digital Object Identifier 10.30941/CESTEMS.2022.00040

investigated through finite element algorithm (FEA) simulation and experiments for different operating conditions. Finally, brief conclusions are drawn in Section V.

II. Mechanism of End Effects in NLS-LDFM

A. Analyzing Assumptions

The analytical model is related to many factors of the NLS-LDFM. In order to simplify the modeling process and highlight the main issues, some proper assumptions are made as follows:

1) The air gap width is modified by Carter's coefficient, and the slot effect is ignored.
2) The iron core loss is ignored.
3) The slot leakage flux is approximately parallel to the slot bottom, and the adjacent slot effect is ignored.
4) The skin effect of the conductor is ignored.

B. Mechanism of Static End Effect

Due to the open core, the magnetic circuit of NLS-LDFM is asymmetric, which causes direct coupling between PW and CW, as well as a negative sequence magnetic field. This phenomenon is defined as static end effect, and the typical characteristics can be analyzed by the flux model.

In brief, the NLS-LDFM is a kind of short primary linear machine (SPLM), and the excitation winding can generate magneto-motive force (MMF) with pulsating component [17], as expressed by

$$F_{Mv}=\left(2N_{ph}k_{wv}\frac{1}{v\pi}\cos\left(\frac{\pi}{\tau}x+\varphi_{Mv}\right)+k_{av,w}N_{ph}\right)i_M \tag{1}$$

where k_{wv} is the winding factor, $k_{av,w}$ the winding factor of pulsating MMF, τ the pole-pitch of winding, N_{ph} stands for series turns per phase, φ_{Mv} and i_M are the spatial flux phase and current of windings, respectively. And the subscript M represents Phase ABC or abc, respectively, in corresponding to PW and CW.

Single-layer and semi-filled double-layer windings are common winding types for the NLS-LDFM. For the single-layer windings, the mutual inductance between PW and CW can be expressed by

$$\begin{aligned}&M_{Aa}=M_{Ab}=-M_{Ac}=M_{direct}\\&\Rightarrow M_{direct}=\frac{\mu_0N_{ph,p}N_{ph,c}k_{av,c}y_cDL}{2\delta_ep_p}=\frac{\mu_0N_{ph,p}N_{ph,c}k_{av,p}y_pDL}{2\delta_ep_c}\end{aligned} \tag{2}$$

where y is coil pitch, δ_e represents air gap width modified by Carter's coefficient, and D is the transverse width of NLS-LDFM. And the subscripts p, c and r signify PW, CW, and NLS, respectively. The phenomenon of energy transfer between different windings without modulation is called direct coupling, which is the concrete manifestation of the static end effect. As shown in (2), the root cause of the direct coupling between PW and CW is the pulsating MMF. And the mutual inductance of primary windings can be derived by

$$\begin{aligned}&M_{sw,AB}=-\frac{L_{sw}^{'}}{2}+L_{sw},M_{sw,AC}=M_{sw,BC}=-\frac{L_{sw}^{'}}{2}-L_{sw}\\&\Rightarrow L_{sw}^{'}=\frac{2\mu_0N_{ph,w}^2k_{wv,w}^2DL}{\delta_e\pi^2v^2},L_{sw}=\frac{\mu_0}{2\delta_ep}Dk_{av,w}N_{ph,w}^2L\end{aligned} \tag{3}$$

where $L_{sw}^{'}$ and L_{sw} are corresponding to traveling and pulsating magnetic field, respectively. It is also clear that the three-phase primary fluxes are symmetrical without L_{sw}. And the three-phase asymmetry coefficient for the single-layer winding with p pole-pairs can be defined as

$$K_{asy}=\frac{2L_{sw}}{L_{sw}^{'}}=\frac{k_{av}\pi^2L}{4k_{wv}^2} \tag{4}$$

For the semi-filled double-layer winding, the phase angle can be expressed by

$$\begin{aligned}&\varphi_A=\frac{(1-3p)(2p-\gamma)\pi}{6p}-\frac{py_c\pi}{Z}+\frac{\pi}{2}\\&\varphi_B=-\frac{(1+3p)(2p-\gamma)\pi}{6p}-\frac{py_c\pi}{Z}+\frac{\pi}{2}\\&\varphi_C=-\frac{(2p-\gamma)\pi}{2}-\frac{py_c\pi}{Z}-\frac{\pi}{2}\\&\Rightarrow\gamma=\frac{2py_c}{Z}\end{aligned} \tag{5}$$

where γ stands for winding pitch ratio, and y_c is the coil pitch in terms of the number of slots, Z the number of primary slots. Then, the phase difference between A and B can be derived as

$$\varphi_A-\varphi_B=\frac{(2p-\gamma)\pi}{3P}=\frac{2\pi}{3}-\frac{2y_c\pi}{3Z} \tag{6}$$

Obviously, $\frac{y_c}{3Z}$ is not an integer. It confirms that the three-phase semi-filled double-layer windings have the phenomenon of flux axis shift. In addition, for one phase of semi-filled slot double-layer windings, the reverse coils generate negative pulsating MMFs that eliminate the positive pulsating MMFs generated by the forward coils. Therefore, the semi-filled double-layer windings cannot generate pulsating MMF, and the flux axis shift is the key cause of direct coupling. Due to the winding asymmetry, the magnetic flux density of PW, CW and NLS have positive and negative components, which can reduce the average thrust of NLS-LDFM.

C. Mechanism of Dynamic End Effect

Based on the principle of magnetic field modulation, the secondary velocity v_r at stable operation satisfies

$$v_r=\frac{f_p\pm f_c}{p_p\pm p_c}L \tag{7}$$

where L is the longitudinal length of NLS-LDFM, f and p are the excitation frequency and pole-pair number of PW or CW, respectively. And the addition or subtraction operators of denominator and numerator depend on the magnetic modulation method and the phase sequence relationship between PW and CW, respectively. And the velocity regulation can be realized by changing the frequency. When the frequency of PW or CW is zero, the NLS-LDFM works at natural synchronous speed. When the current phase-sequence of the two primary windings is the same, the machine operates in the super-synchronous speed region, and when the current phase-sequence is opposite, the machine works in the sub-synchronous speed region.

Assuming that the primary flux density outside the air gap is ignored, the dynamic end effect analysis can be simplified as the computation of zero-state current response or current zero-

input response for NLS-LDFM secondary. The zero-state response circuit for an entry secondary loop can be given in Fig. 2(a), and the zero-input response circuit for an exit secondary loop is shown in Fig. 2(b). As seen from this picture, t_0 is the initial time, R_r the resistance of the secondary loop, $L_{r\sigma}$ the total leakage inductance of the secondary loop, and i_{ren} and i_{rex} are induced current of entry loop and exit loop, respectively.

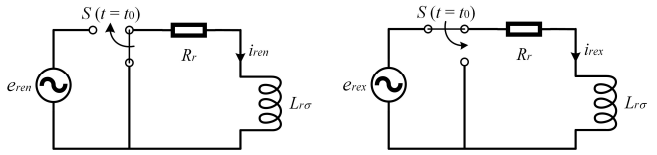

(a) (b)

Fig. 2. The response circuit for a secondary loop. (a) Entry loop circuit. (b) Exit loop circuit.

The relative position between the secondary loop and primary flux can be reflected in the phase angle of EMF e_{ren} and e_{rex}. The transient current for the loop near the entry and exit end can be solved respectively by

$$\begin{cases} L_{r\sigma}\mathrm{p}i_{ren}+R_r i_{ren}+e_{ren}=0 \\ i_{ren}\left(t_0\right)=0 \end{cases} \quad \begin{cases} L_{r\sigma}\mathrm{p}i_{rex}+R_r i_{rex}=0 \\ e_{ex}\left(t_0\right)+R_r i_{rex}\left(t_0\right)=0 \end{cases} \tag{8}$$

where p represents the differential operator about time. Then, the induced current of secondary loop can be derived as

$$\begin{aligned} i_{ren}&=\frac{E_{ren}}{|Z_r|}\left[\cos\left(\omega_r t+\varphi_{ren}-\varphi_Z\right)-\cos\left(\varphi_{ren}-\varphi_Z\right)e^{-\frac{1}{T_{r\sigma}}t}\right] \\ i_{rex}&=i_{rex}\left(t_0\right)e^{-\frac{1}{T_{r\sigma}}t},\ \ T_{r\sigma}=\frac{L_{r\sigma}}{R_r},\ Z_r=R_r+j\omega_r L_{r\sigma} \end{aligned} \tag{9}$$

where φ_{ren} is the initial phase angle of EMF e_{ren}, and φ_Z the impedance angle. In addition, the entry transient component is zero when φ_{ren} is equal to φ_Z. And the transient time constant $T_{r\sigma}$ of loop current is related to secondary leakage reactance parameters, which is relatively large. Thus, the secondary current of entry loop is unable to be generated rapidly.

III. Fundamental Parameters of NLS-LDFM

A. Analysis of Fundamental Functions

To analyze the performance of the NLS-LDFM, it is necessary to investigate the parameters, which contain voltage, flux, and thrust. In a three-phase coordinate system, the voltage and flux functions can be expressed as

$$\begin{aligned} &\begin{bmatrix} \boldsymbol{U}_p \\ \boldsymbol{U}_c \\ \boldsymbol{U}_r \end{bmatrix}=\begin{bmatrix} \boldsymbol{R}_p & \boldsymbol{0} & \boldsymbol{0} \\ \boldsymbol{0} & \boldsymbol{R}_c & \boldsymbol{0} \\ \boldsymbol{0} & \boldsymbol{0} & \boldsymbol{R}_r \end{bmatrix}\begin{bmatrix} \boldsymbol{I}_p \\ \boldsymbol{I}_c \\ \boldsymbol{I}_r \end{bmatrix}+\mathrm{p}\begin{bmatrix} \boldsymbol{\psi}_p \\ \boldsymbol{\psi}_c \\ \boldsymbol{\psi}_r \end{bmatrix} \\ &\Rightarrow\begin{bmatrix} \boldsymbol{\psi}_p \\ \boldsymbol{\psi}_c \\ \boldsymbol{\psi}_r \end{bmatrix}=\begin{bmatrix} \boldsymbol{L}_p & \boldsymbol{M}_{pc} & \boldsymbol{M}_{pr} \\ \boldsymbol{M}_{cp} & \boldsymbol{L}_c & \boldsymbol{M}_{cr} \\ \boldsymbol{M}_{rp} & \boldsymbol{M}_{rc} & \boldsymbol{L}_r \end{bmatrix}\begin{bmatrix} \boldsymbol{I}_p \\ \boldsymbol{I}_c \\ \boldsymbol{I}_r \end{bmatrix} \end{aligned} \tag{10}$$

where $\boldsymbol{U}$, $\boldsymbol{R}$, $\boldsymbol{\Psi}$, $\boldsymbol{L}$, $\boldsymbol{M}$, and $\boldsymbol{I}$ stand for voltage, resistance, flux, self-inductance, mutual inductance, and current matrix, p is the differential operator of time. Then, the thrust function of NLS-LDFM can be obtained by using the principle of Virtual Work, as shown in (11).

$$T_e=\boldsymbol{M}_{cr}=\left(\boldsymbol{I}_p\right)^T\frac{\partial \boldsymbol{M}_{pr}}{\partial x}\boldsymbol{I}_r+\left(\boldsymbol{I}_c\right)^T\frac{\partial \boldsymbol{M}_{cr}}{\partial x}\boldsymbol{I}_r \tag{11}$$

As shown in (10) and (11), it is clear that the voltage, flux, and thrust depend on the inductance parameters of NLS-LDFM. However, due to end effects, the inductance functions of NLS-LDFM are quite different from that of rotary machines. And it is emphatically analyzed in the next parts.

B. Analysis of Inductance in Main Flux Path

Without considering winding leakage inductance, the inductance matrixes of PW and CW can be expressed as

$$\boldsymbol{L}_w=\begin{bmatrix} 1 & -\frac{1}{2} & -\frac{1}{2} \\ -\frac{1}{2} & 1 & -\frac{1}{2} \\ -\frac{1}{2} & -\frac{1}{2} & 1 \end{bmatrix}L'_{sw,p}+\begin{bmatrix} 1 & 1 & -1 \\ 1 & 1 & -1 \\ -1 & -1 & 1 \end{bmatrix}L_{sw,p} \tag{12}$$

where the subscript w stands for the PW or CW. Based on the short primary winding function, the secondary MMF with pulsating component can be defined as

$$F_{r,mn}\left(x\right)=\sum_{v}^{\infty}k_{r,mn}\cos\left[\frac{2\pi v}{L}x+\varphi_{r,mn}\right]i_{r,mn}-k_{av}y_{mn}i_{r,mn} \tag{13}$$

where y_{mn} is the effective loop span, x_{c0} the initial position of the entry nest center-line, τ_r the nest span, t_r represents the movement time of the loop, the subscript n represents the mark number of the loop, and m stands for the mark number of the nest. Moreover, the permeance along the direction of movement is not a constant. The permeance outside the air gap is relatively small to the permeance inside the air gap, so the primary flux density outside the air gap can be ignored. And the numerical expression for the end permeance Λ_{end} can be found by Schwarz-Christoffel mapping [22], as illustrated by

$$\Lambda_{end}\left(x\right)\approx\begin{cases} \frac{\mu_0}{4\delta_e^{\,2}}\left(\sqrt{16\delta_e^{\,2}+\pi^2x^2}+\pi x\right) & x\le 0 \\ \frac{\mu_0}{4\delta_e^{\,2}}\left[\sqrt{16\delta_e^{\,2}+\pi^2\left(x-L\right)^2}-\pi\left(x-L\right)\right] & x\ge L \end{cases} \tag{14}$$

As shown in Fig. 3, it is indicated that the end permeance Λ_{end} tends to decay rapidly with the air gap permeance μ_0/δ_e as the maximum. Besides, the zero point of conductor position is set at the left end of the air gap, and the secondary movement direction is positive in the x-axis, as shown in Fig. 3.

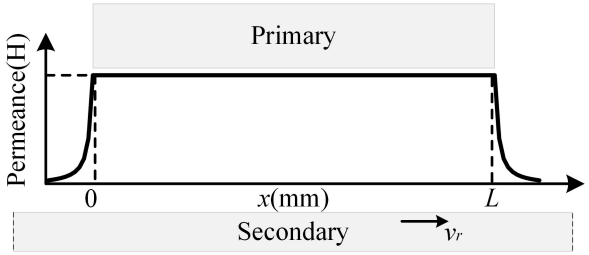

Fig. 3. Permeance characteristic of the LDFM.

Furthermore, the inductance matrixes of the NLS can be derived by

$$\boldsymbol{L}_r=\begin{bmatrix} y_{11}y_{11} & y_{11}y_{12} & \cdots & y_{11}y_{mn} \\ y_{12}y_{11} & y_{12}y_{12} & \cdots & y_{12}y_{mn} \\ \vdots & \vdots & \ddots & \vdots \\ y_{mn}y_{11} & y_{mn}y_{12} & \cdots & y_{mn}y_{mn} \end{bmatrix} L_{rav}+\begin{bmatrix} \alpha_{11,11} & \alpha_{11,12} & \cdots & \alpha_{11,mn} \\ \alpha_{12,11} & \alpha_{12,12} & \cdots & \alpha_{12,mn} \\ \vdots & \vdots & \ddots & \vdots \\ \alpha_{mn,11} & \alpha_{mn,12} & \cdots & \alpha_{mn,mn} \end{bmatrix} L_r \tag{15}$$

$$\Rightarrow L_{rav}=\frac{\mu_0 k_{av} D}{\delta_e}, L_r=\frac{2\mu_0 DL}{\delta_e \pi^2 v^2}, \alpha_{ij,qf}=k_{r,ij}k_{r,qf}\cos\left(\varphi_{r,ij}-\varphi_{r,qf}\right)$$

where the subscript *ij* represents the *j*th loop of the *i*th nest, and the subscript *qf* stands for the *f* th loop of the *q*th nest. What is now clear is that the first and second terms of the inductance matrixes of primary and secondary windings are corresponding to traveling and pulsating magnetic field, respectively. The mutual inductance matrixes between the primary windings and NLS can be expressed by (16), which has the two components corresponding to traveling and pulsating magnetic field, respectively.

$$\begin{aligned} \boldsymbol{M}_{w,r}=\left(\boldsymbol{M}_{r,w}\right)^T&=\begin{bmatrix} y_{11} & y_{12} & \cdots & y_{mn} \\ y_{11} & y_{12} & \cdots & y_{mn} \\ -y_{11} & -y_{12} & \cdots & -y_{mn} \end{bmatrix} M_{rav} \\ &+\begin{bmatrix} \beta_{11,Aw} & \beta_{12,Aw} & \cdots & \beta_{mn,Aw} \\ \beta_{11,Bw} & \beta_{12,Bw} & \cdots & \beta_{mn,Bw} \\ \beta_{11,Cw} & \beta_{12,Cw} & \cdots & \beta_{mn,Cw} \end{bmatrix} M_r \end{aligned} \tag{16}$$

$$\Rightarrow M_{rav}=\frac{\mu_0 N_{ph,w} k_{av,w} D}{\delta_e}, M_r=\frac{2\mu_0 N_{ph,w} k_{wv,w} DL}{\delta_e \pi^2 v^2}$$

$$\Rightarrow \beta_{ij,Mw}=k_{r,ij}\cos\left(\varphi_{r,ij}-\varphi_{M,w}\right)$$

C. Analysis of Inductance in Leakage Flux Path

It is also important to analyze the leakage inductance parameters, which are closely related to operation characteristics. Due to the end effect and specificity of the NLS-LDFM structure, the analysis of leakage inductance is complex. In this part, a generalized method is used for multifarious leakage inductance calculations, which has a reference value for the performance optimization of NLS-LDFM. The calculation of slot leakage inductance can come down to the leakage permeance modeling [18]. The derivation results are various for different slot types. The regional slot leakage permeance calculation model is exemplified by the common slot type of NLS, as shown in Fig. 4.

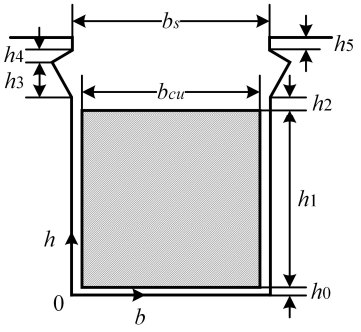

Fig. 4. Regional slot leakage permeance calculation model of the NLS.

It is assumed that relative permeance in the conductor region is the same as in air, and the slot magnetic field intensity H_{slot} is a constant value along the *x*-axis direction. For the region $0 \le h < h_0$, the leakage flux is zero. For the other regions, the leakage permeance can be derivated by Ampere circuit law, taking $h_0 \le h < h_0+h_1$ for example, as shown in (17) and (18).

$$\begin{aligned} H_{rslot}b_s&=\frac{h-h_0}{h_1}I_{slot} \\ \mathrm{d}\phi_{rslot}&=\mu_0\frac{h-h_0}{b_s h_1}I_{slot}l_f\mathrm{d}h \\ \mathrm{d}\psi_{rslot}&=\mu_0\frac{\left(h-h_0\right)^2}{b_s h_1^2}I_{slot}l_f\mathrm{d}h \\ \mathrm{d}L_{rslot}&=\mu_0\frac{\left(h-h_0\right)^2}{b_s h_1^2}l_f\mathrm{d}h=\mathrm{d}\lambda_1 \end{aligned} \tag{17}$$

$$\lambda_1=\mu_0\frac{l_f}{b_s h_1^2}\int_{h_0}^{h_0+h_1}\left(h-h_0\right)^2\mathrm{d}h=\mu_0\frac{l_f h_1}{3b_s} \tag{18}$$

where I_{slot} is the slot current, $l_f\,\mathrm{d}h$ the effective area for the slot leakage flux, and λ_1 stands for the leakage permeance of this region. Identically, for the upper area of current-carrying conductors, the leakage permeance λ_2 can be derived by

$$\begin{aligned} \lambda_2=\mu_0 l_f\Bigg\{&\int_{h_0+h_1}^{h_0+h_1+h_2}\frac{1}{b_s}\mathrm{d}h+\int_{h_0+h_1+h_2+h_3+h_4}^{h_0+h_1+h_2+h_3+h_4+h_5}\frac{1}{b_s}\mathrm{d}h \\ &+\int_{h_0+h_1+h_2}^{h_0+h_1+h_2+h_3}\left[b_s+\frac{2\sqrt{3}\left(h-h_0-h_1-h_2\right)}{3}\right]^{-1}\mathrm{d}h \\ &+\int_{h_0+h_1+h_2+h_3}^{h_0+h_1+h_2+h_3+h_4}\left[b_s+2\sqrt{3}\left(h-h_0-h_1-h_2-h_3\right)\right]^{-1}\mathrm{d}h\Bigg\} \\ =\mu_0 l_f\Bigg\{&\frac{h_2+h_5}{3b_s}+\frac{\sqrt{3}}{6}\ln\left[\frac{\left(3b_s+2\sqrt{3}h_3\right)^3\left(b_s+2\sqrt{3}h_4\right)}{27b_s^4}\right]\Bigg\} \end{aligned} \tag{19}$$

The above leakage permeabilities are paralleled in the magnetic circuit. In such case, the slot leakage inductance of NLS can be expressed by

$$L_{slot}=\lambda_1+\lambda_2 \tag{20}$$

where N_{slot} is the number of series conductors in the slot. The magnetic fluxes outside p_p and p_c pole-pairs are regarded as harmonic components. Thus, the harmonic leakage inductance is formulated as a harmonic flux modeling problem. Combined with (3) and (12), the function of harmonic leakage inductance for one three-phase winding can be expressed as

$$L_{h,w}=\frac{3\mu_0 N_{ph,w}^2 k_{wv,w}^2 DL}{\delta_e \pi^2 v^2} \tag{21}$$

Ignoring the influence of harmonic leakage mutual flux, the harmonic leakage flux of one loop can be derived as

$$\begin{aligned} \psi_{rh,mn}&=\mu_0\frac{D}{\delta_e}\int_{x_{c0}+(m-1)\tau_r-\frac{y_n}{2}+v_r t_r}^{x_{c0}+(m-1)\tau_r+\frac{y_n}{2}+v_r t_r}N_{r,mn}\left(x\right)I_{r,mn}dx \\ &=\mu_0\frac{DI_{r,mn}}{\delta_e}\sum_v\frac{k_{r,mn}L}{2\pi v}\Bigg\{\sin\left[\frac{2\pi v}{L}\left(x_{c0}+\left(m-1\right)\tau_r+\frac{y_{mn}}{2}\right)+\varphi_{r,mn}\right] \\ &\quad-\sin\left[\frac{2\pi v}{L}\left(x_{c0}+\left(m-1\right)\tau_r-\frac{y_{mn}}{2}\right)+\varphi_{r,mn}\right]\Bigg\} \end{aligned} \tag{22}$$

Further, the harmonic leakage inductance of the secondary loop can be expressed by

$$L_{h,c}=\sum_{v=v_\sigma}^{\infty}\frac{\mu_0 D}{2\pi v\delta_e}\left[k_{r,mn}L\left(\sin\varphi_1-\sin\varphi_2\right)-k_{av}\frac{4\pi v y_{mn}^{\ 2}}{L^2}\right]$$
$$\Rightarrow \varphi_1=\varphi_{r,mn}+\frac{2\pi v x_{mn}}{L},\ \varphi_2=\varphi_{r,mn}+\frac{2\pi v\left(x_{mn}-y_n\right)}{L} \quad (23)$$
$$\Rightarrow x_{mn}=x_{c0}+\left(m-1\right)\tau_r+\frac{y_{mn}}{2}+v_r t_r$$

Moreover, the end shape for random coil bundles approximately tends to rectangular, and the end winding leakage inductance can be derived by method of images [19], as shown by

$$L_{nlet}=L_{ew1}+L_{ew2}+\frac{\mu_0}{4\pi}\left(2a_n+y_n\right) \quad (24)$$

where a_n represents the end length of winding, L_{ew1} is the end winding leakage inductance of the loop with primary iron treated as a perfect conductor, and L_{ew2} the end winding leakage inductance of the loop with primary iron treated as air.

IV. Simulation and Experiment

In this part, the FEA simulation and experiments of NLS-LDFM are taken to analyze the machine performance, as shown in Fig. 5. To minimize the secondary space and analyze end effect performance effectively, the NLS-LDFM prototype is designed as arc linear machine. The PW and CW are single-layer windings, and the one secondary nest consists of three coaxial loops. The windings of Primary2 are open-circuited, while the Primary1 is directly powered by the frequency converter. And the secondary of prototype is connected to the permanent magnet synchronous machine (PMSM) through the torque sensor. Moreover, the structural parameters of the FEA model are the same as the experimental prototype, which are mainly given in Table I.

TABLE I
Main Specifications of the NLS-LDFM

Name	Unit	Value
Number of slots	-	48
Number of PW poles	-	2
Number of CW poles	-	4
Single coil turns of PW	-	16
Single coil turns of PW	-	31
Parallel turns of primary windings	-	5
Longitudinal length of primary core	mm	900
Height of primary core	mm	57
Transversal length of LDFM	mm	125
Air gap length	mm	8

The FEA simulation and experiment for natural synchronous mode are taken to analyze the performance of the static end effect. The CW is supplied with 50 Hz and 120 V rms phase voltage, while the PW is open-circuited. The natural synchronous speed is 7.5 m/s under this operating condition, and the line voltage wave and related FFT results are shown in Fig. 6.

Based on the theory of the direct coupling, the frequency of induced voltage is the same as original winding voltage, where the phases of A and B are opposite to C. For the simulation and experiment results, the 50Hz induced line voltages are caused by direct coupling, and the test phases for AB and BC are 115.30° and 119.83°, respectively. And the amplitude and phase differences demonstrate that the direct coupling components for A and B phase voltage are unequal, which causes the 50Hz component for U_{pAB} is not zero. Furthermore, the 100Hz voltage harmonics are induced by the negative-sequence flux of CW. And the test phases for AB, BC, and CA

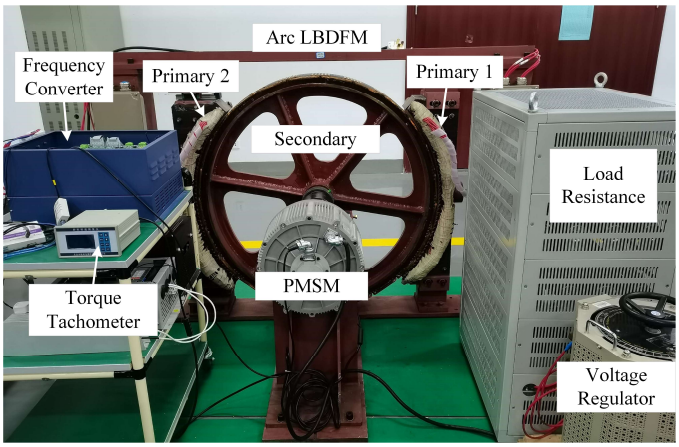

(a)

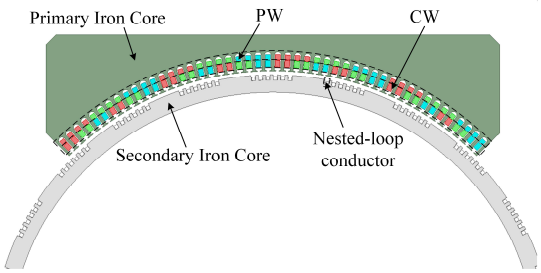

(b)

Fig. 5. The test platform and FEA model for NLS-LDFM. (a) The test platform. (b) The FEA model.

are -142.16°, 101.86°, and -25.57°, respectively. Moreover, the reasons for the difference among theory, simulation, and experiment can be summarized as follows:

1) Due to the permeance of iron core, the relationship between pulsating MMF and coil pitch is nonlinear, which is simplified as the coefficient k_{av} in the theoretical analysis.
2) The NLS-LDFM has low saliency because of the non-uniform distribution of secondary slots, while the slot effect is ignored in the theoretical analysis.
3) The differences between FEA simulation and experiment results are mainly caused by the machine assembly deviation, which leads to non-uniform air gap and intensified the winding asymmetry. Thus, the relevant results of experiment are larger than that of simulation.

In order to further analyze the above performance on static end effect, the experiment for doubly fed mode is carried out. The PW is supplied with 50 Hz and 120 V rms line voltage, while the CW is powered by -20Hz and 54 V rms line voltage. And the negative frequency represents the reverse phase. The NLS-LDFM operates as a motor and drives a 215.7N load at 4.5m/s. The current wave and related FFT results are shown in Fig. 7.

According to the FFT results, the fundamental currents of C phase are relatively small. The 20Hz harmonic current of PW

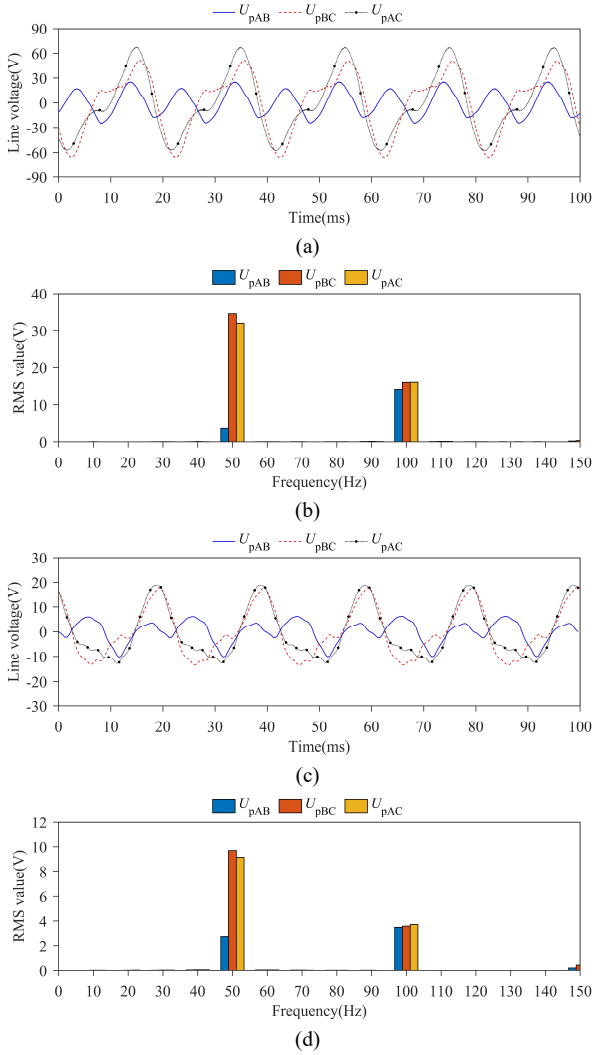

Fig. 6. The FEA simulation and experiment results for natural synchronous mode with open-circuited PW. (a) The test result of PW induced voltage. (b) FFT result of test wave. (c) The simulation result of PW induced voltage. (d) FFT result of simulation wave.

and the 50Hz harmonic current of CW are cause by the direct coupling. Due to the winding asymmetry, the 80Hz harmonic current of CW stems from the secondary modulation of the 50Hz harmonic magnetic field of PW. And 80Hz harmonic current of PW is induced through the direct coupling. All of them are consistent with the above performance analysis.

For the dynamic end effect, the FEA simulation for cascadeasynchronous mode is carried out to analyze the secondary loop current. The NLS-LDFM drives at 9.6 m/s, and the PW is powered by 50 Hz and 180 V rms line voltage, and the CW is short-circuited. The secondary loop current is shown in Fig. 8. The left dashed line stands for the entry boundary, and the right dashed line represents the exit boundary. Due to the end primary flux, the zero-state response current is induced before the loop enters the air gap. When the loop moves out of the air gap, the induced current does not rapidly decay to zero but continues for a period.

Furthermore, another group of FEA simulation and experiment for cascade asynchronous mode is carried out under the symmetrical current excitation. Since the rotary machine has not end effects, the mechanical characteristics are both

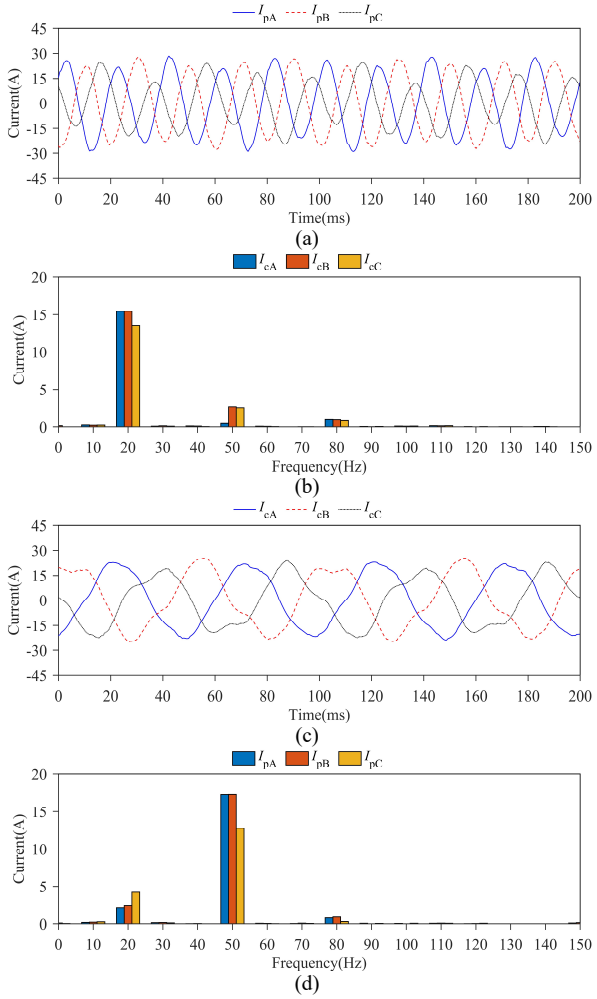

Fig. 7. The experiment results for doubly fed mode. (a) The test result of PW current. (b) FFT result of PW current. (c) The test result of CW current. (d) FFT result of CW current.

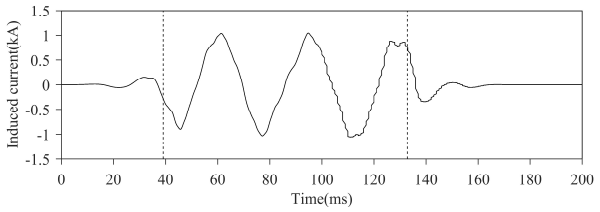

Fig. 8. The induced current for a secondary loop.

simulated for the NLS-LDFM and its corresponding rotary machine, as shown in Fig. 9. The PW is powered by 50 Hz and 19 A rms phase current, and the CW is short-circuited, and the natural synchronous speed is 7.5 m/s calculated by (7). For NLS-LDFM applied in urban rail transit, the boundary value of high-speed and low-speed region is around 11.11 m/s, and the boundary has been marked as the blue dashed line shown in Fig. 9. And the thrust of NLS-LDFM is mainly affected by direct coupling and the dynamic end effect. Based on the theory analysis, the direct coupling is irrelevant to operation speed. Moreover, the transient time constant $T_{r\sigma}$ of secondary loop current is related to the impedance parameters of the NLS. And the loop distribution constant $(L+\tau_r)/v_r$ is inversely proportional to operation speed. Thus, the dynamic end effect on thrust is obviously in the high-speed region, since $T_{r\sigma}$ is relatively large

than the loop distribution constant. And the thrust is mainly affected by direct coupling in the low-speed region, while the dynamic end effect is relatively weak.

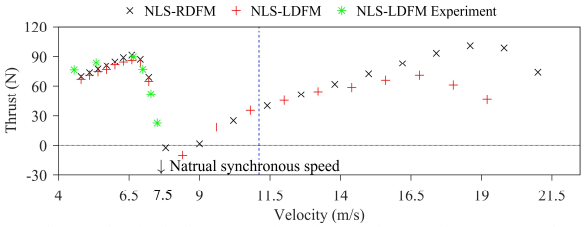

Fig. 9. The mechanical characteristics of cascade asynchronous mode.

V. Conclusions

In this paper, the mechanism of the static and dynamic end effects is analyzed. Furthermore, the performances of NLS-LDFM are also analyzed by FEA simulation and experiments under some typical operating conditions. Main conclusions are drawn as follows.

Winding asymmetry and direct coupling are main manifestations of the static end effect. For the single-layer windings, the pulsating MMF is the root cause of the static end effect. For the semi-filled double-layer windings, the shift of flux axis is the key reason of the static end effect. In addition, the current and voltage of the primary winding contain negative sequence harmonics caused by winding asymmetry.

Besides, the transient secondary current is the main cause of the dynamic end effect. And the zero-state response current and zero-input response current exist in the entry loop and exit loop, respectively. According to the derived transient time constant of secondary loop current, the dynamic end effect can reduce the thrust obviously in the high-speed region.

However, due to the segmentation of effective loop span, the relevant inductance matrixes of NLS are high-dimensional and difficult for order reduction and coordinate transformation. And the quantitative analysis of dynamic end effect is relatively difficult. Next step, the global continuously differential solutions for the NLS parameters should be focused.

References

[1] F. Saifkhani and A. K. Wallace, "A linear brushless doubly-fed machine drive for traction applications," *European Conf. Power Electron. Appl. (EPE)*, pp. 344-348, 1993.

[2] C. Kan, J. Zhang, B. Ma, T. Ren, and G. Chu, "Design and simulation on a new type linear brushless doubly-fed machine," *Micromotors*, vol. 48, no. 12, pp. 11-16, Dec. 2015.

[3] R. Cao and W. Huang, "A double fed three-phase flux-NLSitching linear motor with complementary magnet circuit for urban rail transit," *IEEE Conf. Expo Trans. Electrification Asia-Pacific (ITEC Asia-Pacific)*, pp. 1-5, 2014.

[4] C. Henke, N. Frohleke, and J. Bocker, "Advanced convoy control strategy for autonomously driven railway vehicles," *IEEE Intelligent Trans. Systems Conf. (ITSC)*, pp. 1388-1393, 2006.

[5] T. Schneider, B. Schulz, C. Henke, *et al.*, "Energy transfer via linear doubly-fed motor in different operating modes," *IEEE Int. Electric Mach. and Drives Conf. (IEMDC)*, pp. 598-605, 2009.

[6] H. Grotstollen. "The design of long-stator linear motor drives for railcab test track," *Journal of Power Electronics*, vol. 5, no. 2, pp. 166-172, Apr. 2005.

[7] B. Becetti, "Design and optimization of linear doubly-fed induction machine for wireless charging operation of novel vactrain system," *Ph.D. Dissertation*, TU Delft, Delft, NL, 2021.

[8] Y. Wang, "Research on power generation mode and control system of double-fed linear motor for urban rail," *Ph.D. Dissertation*, NLSJTU, Chengdu, SC, CHN, 2016.

[9] J. Kang, S. Mu, and H. Ding. "Long stator linear doubly-fed motor for high-speed maglev integrated suspension, propulsion and contactless power supply," *Int. Symp. on Linear Drives for Ind. Appl. (LDIA)*, pp.1-5, 2021.

[10] M. Chen, L. Wu, L. Zhang, *et al.*, "A novel doubly-fed flux reversal linear machine with armature windings wound on both stator and mover teeth," *IEEE Access*, vol. 8, pp. 35563-35571, Feb. 2020.

[11] L. Wu, L. Zhang, J. Zhu, *et al.*, "Comparative study of novel doubly-fed linear NLSitched flux permanent magnet machines with different primary structures," *IEEE Access*, vol. 8, pp. 69401-69412, Apr. 2020.

[12] W. Xu, R. Islam, and M. Pucci, *Advanced Linear Machines and Drive Systems*, Springer-Verlag Berlin Heidelberg, Sep. 2019.

[13] I. Boldea, L. Tutelea, W. Xu, and M. Pucci, "Linear electric machines, drives and MAGLEVs: an overview," *IEEE Trans. Ind. Electron.*, vol. 65, no. 9, pp. 7504-7515, Sep. 2018.

[14] W. Xu, G. Sun, G. Wen, Z. Wu, and P. K. Chu, "Equivalent circuit derivation and performance analysis of a single-sided linear induction motor based on the winding function theory," *IEEE Trans. Veh. Technol.*, vol. 61, no. 4, pp. 1515-1525, May 2012.

[15] W. Xu, X. Xiao, G. Du, D. Hu, and J. Zou, "Comprehensive efficiency optimization of linear induction motors for urban transit," *IEEE Trans. Veh. Techno.*, vol.69, no.1, pp.131-139, Jan. 2020.

[16] Y. Zhao, X. Xiao, and W. Xu, "Accelerating optimal shape design of linear machines by transient simulation using mesh deformation and mesh connection techniques," *IEEE Trans. Ind. Electron.*, vol.65, no.12, pp. 9825-9833, Dec. 2018.

[17] J. Ge, W. Xu, Y. Liu, F. Xiong, and D. Li, "Investigation on winding theory for short primary linear machines," *IEEE Trans. Veh. Technol*, vol. 70, no. 8, pp. 7400-7412, Aug. 2021.

[18] C. Kan, H. Li, T. Ren, *et al.*, "Calculation of leakage inductance for wound-rotor brushless doubly-fed machine," *Transactions of China Electrotechnical Society*, vol.34, no.19, pp. 4017-4027, Oct. 2019.

[19] T. A. Lipo, "Use of magnetic circuits in leakage reactance calculations," *Introduction to AC Machine Design*, *IEEE*, 2018, pp.161-201.

[20] J. Ge, W. Xu, F. Xiong, Y. Liu, and K. Yu, "Magnetic field analysis of linear brushless doubly-fed machine," *Int. Conf. Electrical Machines and Systems (ICEMS)*, pp. 1894-1898, 2018.

[21] J. Ge, W. Xu, Z. Bao and Y. Zhang, "Analysis of end effect on thrust ripple in linear brushless doubly-fed machine," *Int. Electrical Engineering Congress (iEECON)*, pp. 1-4, 2022.

[22] T. C. O'Connell and P. T. Krein, "A schwarz–christoffel-based analytical method for electric machine field analysis," *IEEE Trans. Energy Convers.*, vol. 24, no. 3, pp. 565-577, Sept. 2009.

Yaping Zhang was born in Shandong, China, in 1999. She received the B.E. degree in electrical engineering and automation from Northeast Forestry University, Harbin, China, in 2021.

She is currently working toward the M.E. degree in electrical engineering in Huazhong University of Science and Technology. Her research interests include linear machines, and brushless doubly-fed machines.

Jian Ge was born in Heilongjiang, China, in 1994. He received the B.E., M.E. and Ph.D degrees in electrical engineering from Huazhong University of Science and Technology, Wuhan, China, in 2016, 2019 and 2022, respectively.

He is currently a Postdoctoral Researcher in electrical engineering in Huazhong

University of Science and Technology. His research interests include induction machines, linear machines, and brushless doubly-fed machines.

Wei Xu (M'09-SM'13) received the double B.E. and M.E. degrees from Tianjin University, Tianjin, China, in 2002 and 2005, and the Ph.D. from the Institute of Electrical Engineering, Chinese Academy of Sciences, in 2008, respectively, all in electrical engineering. His research topics mainly cover design and control of linear/rotary machines. From 2008 to 2012, he made Postdoctoral Fellow with University of Technology Sydney, Vice Chancellor Research Fellow with Royal Melbourne Institute of Technology, Japan Science Promotion Society Invitation Fellow with Meiji University, respectively.

Since 2013, he has been Full Professor with State Key Laboratory of Advanced Electromagnetic Engineering in Huazhong University of Science and Technology, China. He has more than 110 papers accepted or published in IEEE Transactions Journals, two edited books published by Springer Press, one monograph published by China Machine Press, and around 150 Invention Patents granted or pending, all in the related fields of electrical machines and drives. He is Fellow of the Institute of Engineering and Technology (IET). He is the General Chair for 2021 International Symposium on Linear Drives for Industry Applications (LDIA 2021) and 2023 IEEE International Conference on Predictive Control of Electrical Drives and Power Electronics (PRECEDE 2023), in Wuhan, China, respectively. He has served as Associate Editor for several IEEE Transactions Journals, such as IEEE Transactions on Industrial Electronics, IEEE Transactions on Vehicular Technology, IEEE Transactions on Energy Conversion, and so on.

Weiye Li received the B.E. degree from the School of Automation and Information Engineering, Xi'an University of Technology, Xi'an, China, in 2009. He received the M.E. degree from the School of Electrical Engineering, Xi'an Jiaotong University, Xi'an, China, in 2012. He has joined Xiangyang CRRC Motor Technology Co., Ltd., since 2012. He has been engaged in the research and product development of permanent magnet machine and linear machine and drive system.

Yinglu Luo received the B.E. degree from the School of Mechanical Design, Manufacturing and Automation, Xi'an University of Electronic Science and Technology, Xi'an, China, in 2009. He has joined the CRRC Zhuzhou Institute CO., LTD from 2009 and he has been engaged in the research and product development of permanent magnet machine and linear machine.

Shihu Su received the master degree from the School of Electrical and Electronic Engineering, Huazhong University of Science and Technology, China, in 2017. He is now working with CRRC Zhuzhou Motor Co., Ltd., Zhuzhou, China, where he is responsible for the research and product development of linear machines and drives.

Yunfeng He received the Ph.D. degree with Zhejiang University in electrical engineering in 2014. He is one Professorate Senior Engineer and Director of Maglev Product Research Institute of CRRC Zhuzhou Motor Co., Ltd., Zhuzhou, China. He has mainly focused on the research and development of traction motor for rail transit and drives. He is responsible for the development of China's first metro train, the first intercity electric multiple unit (EMU), 863 project high-speed EMU, and Fuxing 160 km/h power centralized EMU.